# 18

# Micromachined Arrayed Capacitive Ultrasonic Sensor/Transmitter with Parylene Diaphragms

Seiji Aoyagi
*Kansai University*
*Japan*

## 1. Introduction

For the external environment recognition of a robotic field, an ultrasonic sensor has advantages in cost performance compared with other sensors such as vision devices. In particular, in the spaces where vision devices cannot be used (e.g., in the dark, smoky situation such as in the disaster site), ultrasonic sensors are effective. For the purpose of using ultrasonic devices in microrobot applications (Aoyagi, 1996), and/or for the purpose of imitating the dexterous sensing functions of animals such as bats and dolphins (Mitsuhashi, 1997; Aoyagi, 2001), it is necessary to miniaturize the current ultrasonic sensors/transmitters (Haga et al., 2003).
The effectiveness of miniaturization is discussed herein from the viewpoint of directivity. Let us assume a piston-type ultrasonic device, the radius of which is $R$. The angle $\theta_{1/2}$ at which the sound pressure level becomes half of the maximal level achieved on the centerline of the piston ($\theta$ =0) is expressed as follows (Mitsuida, 1987):

$$\theta_{1/2} = \sin^{-1}(0.353\lambda / R) , \tag{1}$$

where $\lambda$ is the wavelength. The schematic explanation of this angle is shown in Fig. 1. This equation indicates that directivity becomes wider as the radius becomes smaller. Using many miniaturized transmitters/sensors in an array, the electrical scanning of directivity based on the delay-and-summation principle (Fig. 2) (Ono et al., 2005; Yamashita et al., 2002a; Yamashita et al., 2002b) and acoustic imaging based on the synthesis aperture principle (Guldiken & Degertekin, 2005) are possible, which could be effectively used for robotic and medical applications. Miniaturizing one sensing/transmitting element is useful both for realizing an arrayed device in a limited space and for realizing a device with omnidirectional characteristics, since the directivity of each element becomes wider as its diaphragm area becomes smaller based on equation (1).
There are two types of available ultrasonic sensor, one is piezoelectric, and another is capacitive. The working principle and the typical received waveform of piezoelectric type are schematically shown in Fig. 3. This type is further classified to thin film type and bimorph type. The former uses a micromachined thin film as a diaphragm, on which piezoelectric material such as lead zirconate titanate (PZT) is deposited using sol-gel method or sputtering. The latter uses a rather thick bulk plate as an elastic body of receiving and/or transmitting ultrasound. In case of the thin film type, piezoelectric constant $d_{31}$ is rather

Source: Solid State Circuits Technologies, Book edited by: Jacobus W. Swart,
ISBN 978-953-307-045-2, pp. 462, January 2010, INTECH, Croatia, downloaded from SCIYO.COM

small, so it can act only as a receiver and cannot transmit ultrasound. Although the bimorph type can transmit ultrasound, its size is comparatively large.

The merit of these piezoelectric types is that they do not require bias voltage for their operation. The drawback of piezoelectric types is that the received waveform is burst one, i.e., the waveform continues during several tens cycles, since they are usually operated at their resonant frequencies with small damping. In the ranging system for airborne use (see Section 4.5), the precise arrival time of the ultrasound is difficult to detect for the burst waveform with dull rising, since the first peak is difficult to detect by setting a threshold level.

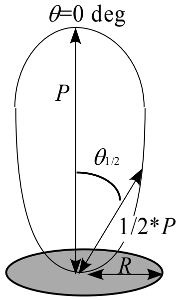


Fig. 1. Definition of $\theta_{1/2}$.

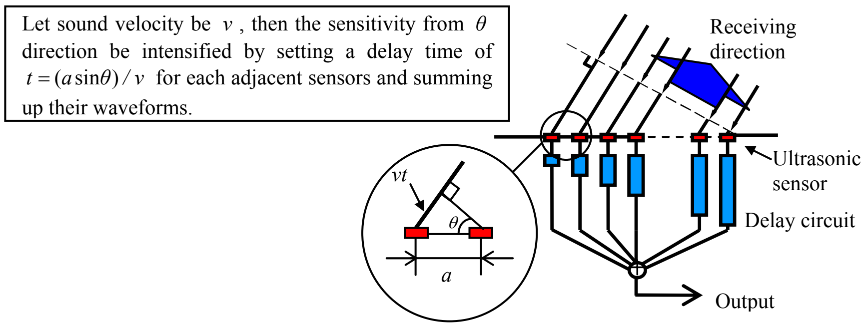


Fig. 2. Electrical scanning of directivity.

By contrast, although the capacitive type needs bias voltage for its operation, it can detect the arrival time of ultrasound accurately by setting an appropriate threshold level, since the received waveform is impulsive and well-damped, as schematically shown in Fig.4. A capacitive sensor can also act as a transmitter by applying an impulsive high voltage between two electrodes (Sasaki & Takano, 1988; Diamond et al., 2002), i.e., a diaphragm and a backing plate, both of which are conductive or coated by thin metal films.

As an example of conventional commercially available capacitive microphones, B&K-type 4138 (Brüel & Kjær, 1982) can receive sound pressure in the ultrasonic frequency range, and can be approximated to be nondirectional by virtue of the small area of its diaphragm. The structure of this microphone is shown in Fig. 5. The diameter, sensitivity, and frequency bandwidth of this microphone are 1/8 in. (3.175 mm), 0.9 mV/Pa, and 100 kHz, respectively. However, this microphone has the drawback of being expensive due to its complicated and precise structure, i.e., it is composed of a thin nickel diaphragm of 1.6 μm thickness, a support rim, and a nickel backing plate facing the diaphragm surface with a small gap of 20 μm.

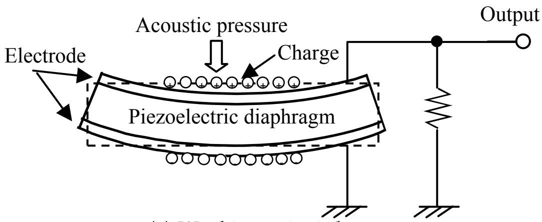


(a) Working principle

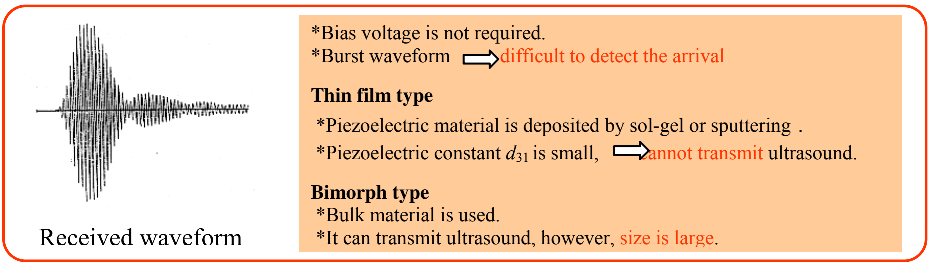


(b) Typical received waveform

Fig. 3. Piezoelectric type ultrasonic sensor.

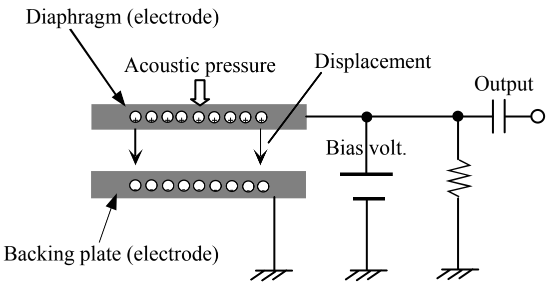


(a) Working principle

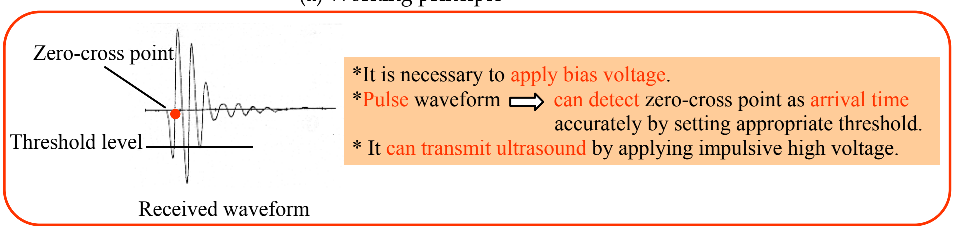


(b) Typical received waveform

Fig. 4. Capacitive type ultrasonic sensor.

A capacitive sensor can also transmit ultrasound by applying impulsive high voltage as mentioned above: however, this B&K microphone is not applicable for the use of a transmitter because of the possibility of diaphragm fracture, taking into account its high cost.
In contrast, several studies on a capacitive microphone with a silicon diaphragm (Scheeper et al., 1992; Bergqvist & Gobet, 1994; Ikeda et al., 1999; Chen et al., 2002; Martin et al., 2005; Khuri-Yakub et al., 2000; Zhuang et al., 2000) have been conducted using micromachining technology (Kovacs, 1998), and some of them have been commercialized (Knowles Acoustics, 2002). Using this technology, numerous arrayed miniaturized ultrasonic sensors with uniform performance can be fabricated on a silicon wafer with a fine resolution of several microns and a comparatively low cost, which may make it possible to fabricate an arrayed-type sensor (Yamashita et al., 2002a; Yamashita et al., 2002b; Guldiken & Degertekin, 2005; Khuri-Yakub et al., 2000; Zhuang et al., 2006) and to activate it as a transmitter or speaker (Diamond et al., 2002; Khuri-Yakub et al., 2000).

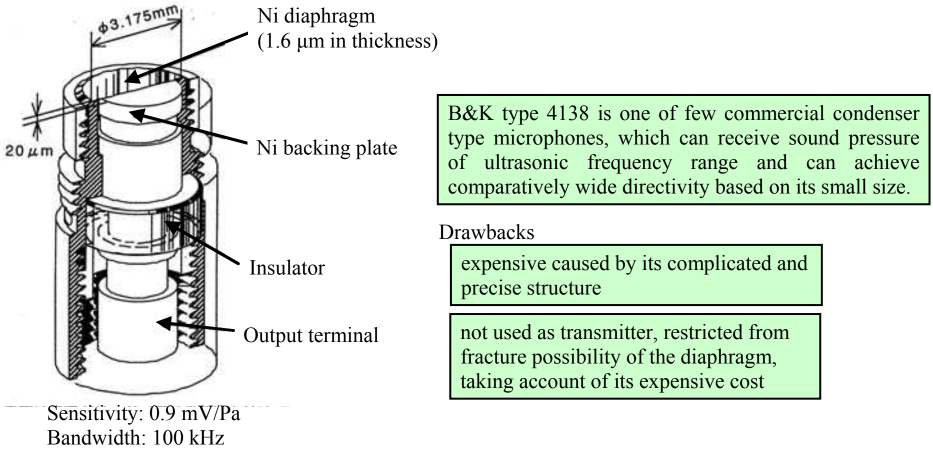


Fig. 5. Stracture of Brüel & Kjær 4138 microphone.

In micromachined capacitive microphones, the diaphragms are generally made of a silicon-based material, such as polysilicon and silicon nitride. In a few studies a polymer material was used for the diaphragms, such as polyimide (Pederson et al., 1998; Schindel et al., 1995), poly(tetrafluoroethylene) (trade name: Teflon) (Hsieh et al., 1999), and poly(ethylene terephthalate) (PET; trade name: Mylar) (Schindel et al., 1995). Since polymer materials have high durability due to their flexibility and nonbrittleness compared with silicon-based materials, their use in transmitters or speakers is thought to be possible. That is, the possibility of survival of a polymer diaphragm would be higher compared with that of a silicon diaphragm even when the applied high impulsive voltage for transmission passes instantaneously over the collapse voltage (Yaralioglu et al., 2005), at which the diaphragm is strongly pulled by an electrostatic attractive force to adhere to the substrate, causing the collapse of the device structure. Since a large displacement of the diaphragm per sound pressure is obtained due to the flexibility of the polymer diaphragm, the high sensitivity of the microphone can be realized. This is because the mechanical impedance of the diaphragm theoretically becomes low as the Young's modulus of the diaphragm's material decreases, provided that the radius, thickness, and input frequency are constant (Khuri-Yakub et al., 2000).

An ultrasonic transducer with a Mylar diaphragm has been commercialized (MicroAcoustic Instruments, trade name: BAT), and is often used in the ultrasonic research field (Hayashi et al., 2001); however, although the pits on the backing plate of this transducer are fabricated by micromachining technology, the polymer diaphragm film is assembled by pressing it to the backing plate with adequate pre-tension using a holder, the assembly of which appears as complicated as that of the above-mentioned B&K-type 4138 microphone.

Polyparaxylene (trade name: Parylene) is one of the polymer materials expected to be applied in the polymer micro-electro-mechanical-systems (MEMS) field (Tai, 2003). The deposition of Parylene is based on chemical vapor deposition (CVD), which is suitable for MEMS diaphragm fabrication. The mechanical properties of silicon, silicon nitride, Parylene, and Mylar are compared, as shown in Table 1. In addition to its flexible and nonbrittle characteristics compared with common polymer materials, Parylene has several excellent characteristics as follows. 1) It is a biocompatible material, which allows medical applications of the device. 2) It is chemically stable, i.e., it has high resistivity to acid, base, and organic solvents, which protects the device from external chemical environments. 3) It has high complementary metal oxide semiconductor (CMOS) compatibility compared with other polymer materials, since it can be deposited at room temperature. This characteristic makes the integration of a device with electrical circuits possible; such a device is called a smart device. 4) Its CVD deposition is conformal, thus the deposition of a domeshaped diaphragm is possible, which is effective for realizing a real spherical sound source/receiver. Due to these characteristics, an ultrasonic device utilizing a Parylene diaphragm has great potential in future applications. The principal aim of this study is to develop a capacitive microphone with a Parylene diaphragm (Aoyagi et al., 2007a).

| | Young's modulus (GPa) | Shear modulus (GPa) | Density (kg/m$^3$) | Poisson ratio |
|---|---|---|---|---|
| Silicon*1 | 131 | 80 | 2,330 | 0.27 |
| Silicon nitride*2 | 290 | — | 3,290 | 0.27 |
| Parylene | 3.2 | — | 1,287 | 0.4 |
| PET (Mylar) | 2.8 | — | 1,370 | 0.4 |

*1 Crystal silicon in (100) plane.
*2 LP CVD $Si_3N_4$ (Tabata et al., 1989).
— Not cleared.

Table 1. Comparison of mechanical properties of silicon and polymer materials.

The reported capacitive microphones focus on audio applications, in which bandwidth is below 15-20 kHz, where the important issues include sensitivity, linearity, and noise floor. In contrast, the present Parylene transducer focuses on ultrasonic applications in air, in which bandwidth is as high as 100 kHz, where the important issue is the accuracy of the distance measurement between the transmitter and the receiver. The directivity of the sensor is also the important issue in these applications. The second aim of this research is to characterize the fabricated Parylene ultrasonic receiver from the viewpoints of the accuracy of distance measurement and the directivity (Aoyagi et al., 2007a).

As the third aim of this research, an arrayed sensor device comprising 5×5 developed sensors is fabricated, and its receiving performance is characterized to prove the possibility of the electrical scanning of directivity based on delay-and-summation principle (Aoyagi et al., 2008a). As the fourth aim of this research, we confirm that each developed sensor can act as a transmitter by applying a high impulsive voltage, which means that the scanning of transmitting directivity is also possible. In this research, the scanning performance as the arrayed transmitter is also characterized (Aoyagi et al., 2008b).

## 2. Structure design of a sensor with Parylene diaphragm

### 2.1 Resonant frequency considering intrinsic stress

The resonant frequency of a Parylene diaphragm is investigated to define the size of the sensor and the bandwidth herein. The shape of the diaphragm is assumed to be a circle. Since Parylene has intrinsic tensile stress influenced by the temperature history of the fabrication (Harder et al., 2002), the relationship between the tensile stress and the resonant frequency is investigated herein.

Assume that the diaphragm has membrane characteristics, in which internal tensile stress plays an important role. Then, the following theoretical expression exists according to the theory of elastic vibration (Sato et al., 1993):

$$\omega_n = \lambda_{ns} \frac{1}{R} \sqrt{\frac{\sigma}{\rho}} , \tag{2}$$

where $\omega_n$ is the resonant frequency (rad/s), $\lambda_{ns}$ is the eigenvalue (2.405), $\sigma$ is the intrinsic tensile stress in the diaphragm ($N/m^2$), $\rho$ is the density of the diaphragm material ($kg/m^3$), and $R$ is the radius of the diaphragm (m).

In FEM (Finite Element Method) simulation, $\sigma$ is applied in the cross section area of the boundary, i.e., the rim, which stretches the diaphragm. The modal FEM simulation is carried out for this stretched diaphragm. ANSYS is employed as the FEM software. In case the diaphragm radius $R$ is 500 μm, theoretical and FEM simulated values of resonant frequency are obtained by changing the value of tensile stress in the range of 0-30 MPa. The result is shown in Fig. 6. This result shows that the influence of tensile stress on the resonant frequency is large. In the following part of this paper, it is assumed that the tensile stress $\sigma$ is 25 MPa, based on the experimental data using rotation tip measurement (see Section 3.2). Under this condition, the relationship between the radius and the resonant frequency is shown in Fig. 7. Considering that the aimed bandwidth is in the ultrasonic range of 40-100 kHz, a radius $R$ in the range of 500-1,200 μm is employed in this research according to this figure.

### 2.2 Influence of acoustic holes on damping ratio

In microphones, acoustic holes are generally set in the backing plate to control air damping. In the case of a simple square diaphragm, the viscous damping coefficient is calculated analytically (Scheeper et al., 1992; Bergqvist & Gobet, 1994; Škvor, 1967) in relation to the number of acoustic holes and to the surface fraction occupied by the acoustic holes. However, there has been no research on air damping for an arbitrary diaphragm shape. Thus, the damping ratio of a circular diaphragm is simulated using the FEM software.

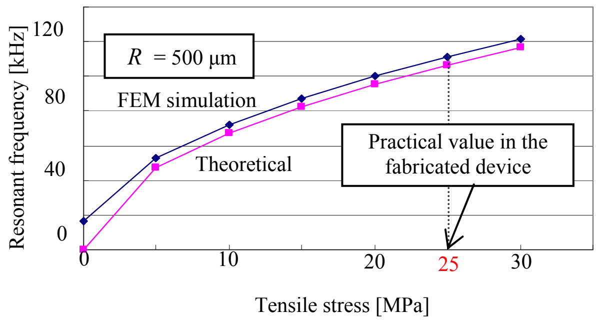


Fig. 6. Relationship between tensile stress and resonant frequency.

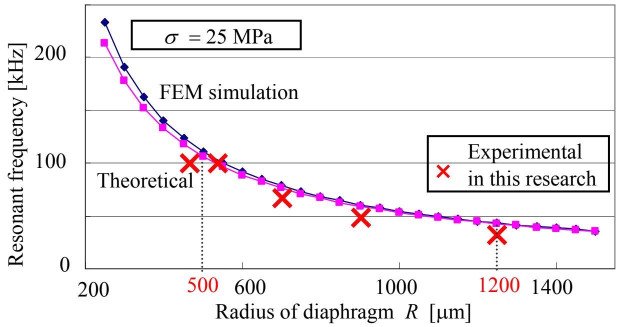


Fig. 7. Relationship between diaphragm radius and resonant frequency.

The flow distribution inside the air gap between the diaphragm and the backing plate, and the flow distribution inside the acoustic holes are simulated by FEM. Taking symmetry into account, a quarter model is employed. An example of the simulation model and its result are shown in Fig. 8. The transition of the displacement distribution, which is based on the first-order resonant vibration mode of a circular diaphragm, was given to the diaphragm. Then, the distribution of vertical flow velocity under the diaphragm was simulated. Total force $F$ was obtained by summing up the pressures of all the elements just below the diaphragm. Flow velocity $u^*$ was obtained by averaging the velocities of all the elements inside the air gap. Then, the damping ratio $\zeta$ was obtained as follows:

$$\zeta = \frac{\lambda}{2m\omega_n} = \frac{F / u^*}{2m\omega_n} \quad , (3)$$

where $m$ is the mass of the diaphragm, $\omega_n$ is the resonant frequency of the diaphragm, $\lambda$ is the viscous damping coefficient.

The effects of the radius of the acoustic hole $r$ and the number of holes $n$ on the damping ratio $\zeta$ were investigated. The simulation result is shown in Fig. 9. Three cases in which the radii of the diaphragm ($R$) were 500, 700, or 1,200 μm are focused on. Considering the practical fabrication condition, the air gap and thickness of the backing plate are assumed to be 1.5 and 150 μm, respectively.

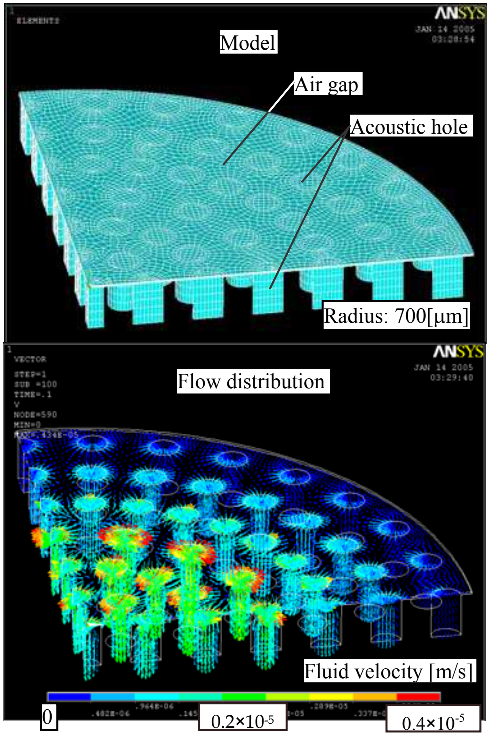


Fig. 8. FEM simulation for influence of acoustic holes on damping ratio.

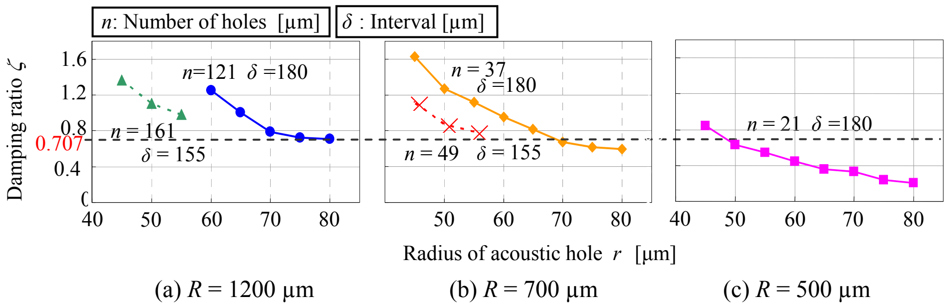


Fig. 9. Damping ratio by FEM simulation.

Also, considering the practical fabrication condition, several combinations of $r$ and $\delta$ (the interval of adjacent acoustic holes) are tested to realize the optimal damping ratio of $\zeta = 1/\sqrt{2}$ =0.707 through trial and error.

In this figure, the damping ratio $\zeta$ is inversely proportional to $r$ and $n$. Also, $\zeta$ decreases as $R$ decreases, indicating that air damping is less effective for smaller diaphragms. For example, in the case of $R$ =1,200 µm, the condition in which $n$ =121 and $r$ =80 µm with $\delta$ = 180 µm is suitable for realizing the optimal damping ratio. Photomasks for a micromachining fabrication of the sensor structure including acoustic holes are designed on the basis of the simulation results explained herein.

## 3. Fabrication process of a sensor

### 3.1 Fabrication process

The ultrasonic sensor was fabricated by depositing Parylene (2 µm in thickness) on a Si wafer (150 µm in thickness) with a thermally grown oxide (1 µm in thickness). Parylene deposition was based on chemical vapor deposition (CVD), and a coating apparatus (PDS-2010, Specialty Coating Systems) was used. The schematic overview of the developed sensor is shown in Fig. 10. The process flow is shown in Fig. 11 and proceeded as follows:

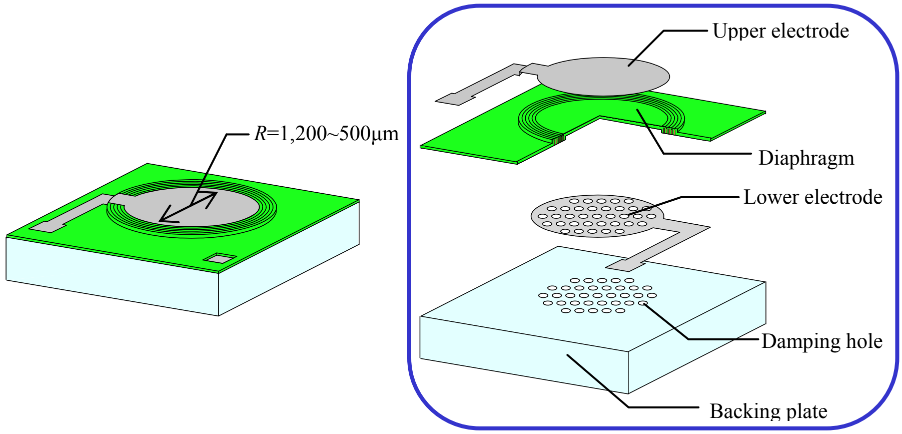


Fig. 10. Schematic overview of parylene ultrasonic sensor.

Aluminum (0.2 µm in thickness) was sputtered onto the oxidized silicon wafer, and patterned for the lower electrode and the bonding pad (see Fig. 11(1)).
As a sacrificial layer, amorphous silicon (1.5 µm in thickness) was deposited by plasma-enhanced CVD, followed by etching using $SF_6$ plasma to make slots, the function of which is explained later (see Fig. 11(2)).
The Parylene (2 µm in thickness) layer was deposited and patterned using $O_2$ plasma to reveal a bonding pad area (see Fig. 11(3)). In this patterning, a photoresist of 5 µm (AZP-4903) was used as the etching mask. Since the etching ratios of Parylene and the photoresist are almost the same, the mask made of the photoresist is gradually consumed during $O_2$ plasma etching. Therefore, a rather thick photoresist was employed.
The slots on the amorphous Si layer were filled with Parylene, providing anchor contact between Parylene and the substrate. Considering the mechanical strength at the edge of the diaphragm, it is desirable that the height of Parylene is the same at the anchor and the diaphragm. If the anchor contact area is large, the height of Parylene at the anchor will be smaller than that at the diaphragm by the thickness of the sacrificial layer, as schematically

shown in Fig. 12(a). To cope with this problem, slots were created and the anchor contact area was minimized. The height of the anchor was maintained at the same level as that of the diaphragm, since Parylene deposition is so conformal as to fill up these slots, as schematically shown in Fig. 12(b). The shapes and sizes of the slots for the anchor are shown in Fig. 12(c).

Aluminum (0.5 μm in thickness) was sputtered and patterned for the upper electrode using the liftoff process. This electrode must surpass the step height of Parylene and amorphous silicon layer (totally 3.5 μm in thickness) to reach the bonding pad, so a comparatively thick aluminum layer is necessary (see Fig. 11(4)).

The backside of the silicon wafer was dry etched by Inductively-Coupled Plasma Deep Reactive Ion Etching (ICP-DRIE) to produce acoustic holes (see Fig. 11(5)). These holes also play a role as the etching holes for the sacrificial amorphous silicon layer, inside which $XeF_2$ etching gas was later introduced.

The oxide layer at the bottom of the acoustic holes was etched using $CHF_3$ plasma (see Fig. 11(6)). The sidewalls of the acoustic holes were covered by Parylene (1 μm in thickness) to protect them from the $XeF_2$ etching gas used later. The conformal deposition of Parylene assists this process (see Fig. 11(7)). The Parylene at the bottom of the holes was etched using $O_2$ plasma. The vertical etching characteristic of the reactive ion etching (RIE) assists the selective etching of the bottom area.

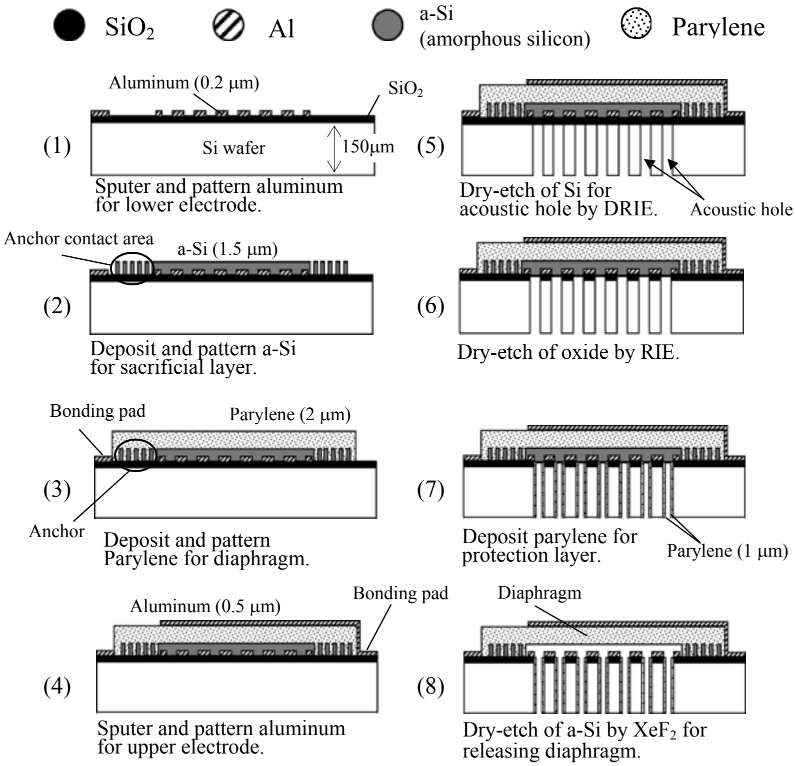


Fig. 11. Process flow of ultrasonic sensor.

Finally, the sacrificial amorphous silicon layer was dry etched away using $XeF_2$ gas in order to release the diaphragm (see Fig. 11(8)). This dry etching process is effective for preventing stiction (Yao et al., 2001).

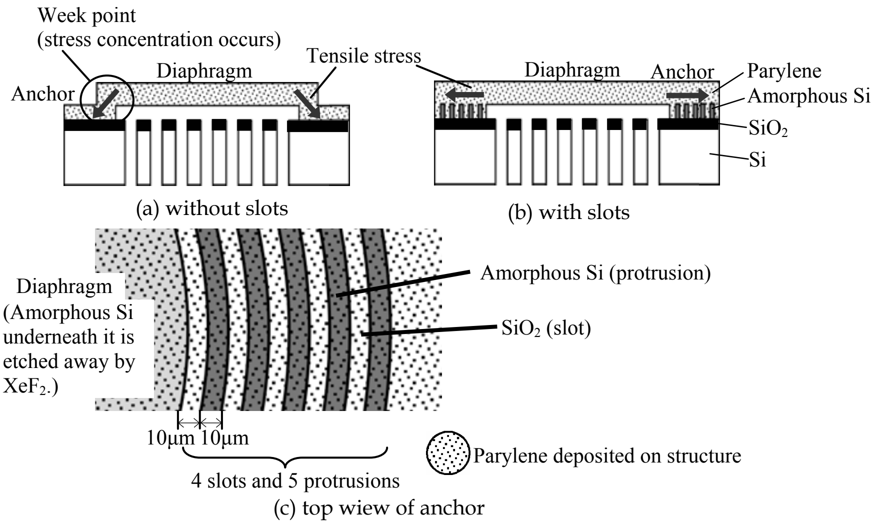


Fig. 12. Reducton of stress concentration using slots.

### 3.2 Fabrication results and intrinsic stress

An overview and schematic cross section of the fabricated sensor are shown in Fig. 13. Scanning Electron Microscope (SEM) images of fabricated sensors are shown in this figure. In this example, the radius of the diaphragm is 1,200 µm, and that of the acoustic hole is 50 µm. Looking at the back-side and cross section views of SEM images, it is proven that the acoustic holes were successfully fabricated. In the front-side view of SEM image, the Parylene circular diaphragm over the acoustic holes is seen. The aluminum upper electrode crossing the anchor is seen.

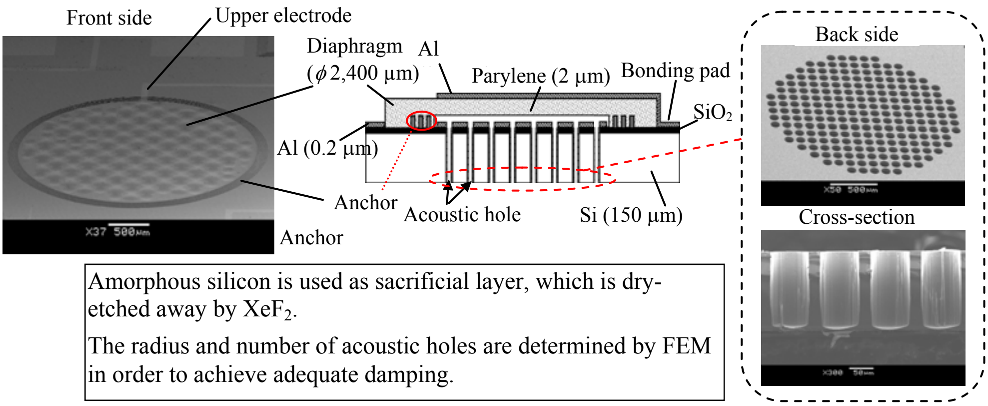


Fig. 13. Overview and schematic cross section of fabricated sensor.

A rotation tip was fabricated in the same substrate in order to estimate the actual tensile stress of Parylene, as shown in Fig. 14. The shrinkage of the beams supporting the tip is $H \cdot \tan\alpha$, and the strain in the film is calculated as $H \cdot \tan\alpha / (L_A + W + L_B)$, using symbols in Fig. 14. Multiplying the strain by Young's modulus of Parylene (3.2 GPa), the stress is obtained, which is proven to be approximately 25 MPa.

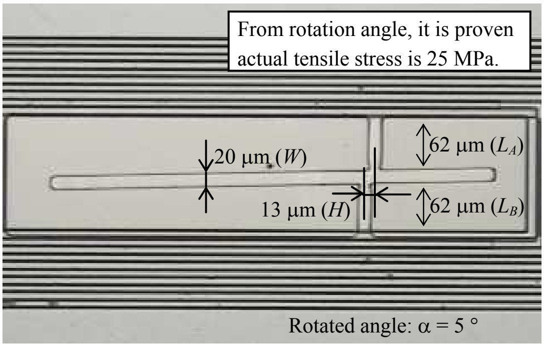


Fig. 14. Optical image of rotation tip.

## 4. Receiving performance of a sensor

### 4.1 Detecting circuitry for capacitance change

The circuitry used to detect the capacitance change due to the diaphragm displacement caused by ultrasonic sound pressure is documented herein. A bias voltage of 100 V was applied to the fabricated Parylene capacitive sensor. This value has an effect on the sensitivity, resonant frequency, and bandwidth (Schindel et al., 1995; Yaralioglu et al., 2005). In this study, this value is defined on the basis of values in references, in which 150 V (Sasaki et al., 1988), 100 V (Khuri-Yakub et al., 2000), 100-400 V (Schindel et al., 1995), and 50-135 V (Yaralioglu et al., 2005) were employed. In this study, the values of 150 and 200 V were experimentally tested; however, it was observed that the diaphragm was broken when a high impulsive voltage of 700 Vpp was applied during the transmitter use (the detail of which is explained in Section 6), although this failure rate is small. Thus, considering the safety factor, the value of 100 V was employed, under which condition neither diaphragm failure nor the disconnection of wiring was encountered.

Upon being supplied with a constant electrical charge due to the bias voltage, the diaphragm displacement was transformed to the voltage change at the sensor's electrode, and it was amplified by a factor of 30 (29.5 dB). The circuitry used for capacitance-to-voltage (CV) transformation and amplification is shown in Fig. 15, in which the high-frequency component of the voltage change is extracted by a bias-cut condenser, and it is input to an operational amplifier by a shunt resistor. Only the range within ±0.7 V is dealt with for amplification by virtue of a voltage limiter using two diodes, considering noise reduction.

### 4.2 Experimental setup for characterizing receiving performance

The experimental setup for characterizing the receiving performance of the developed sensor is schematically shown in Fig. 16. An electric spark discharge was used as an ultrasonic transmitter.

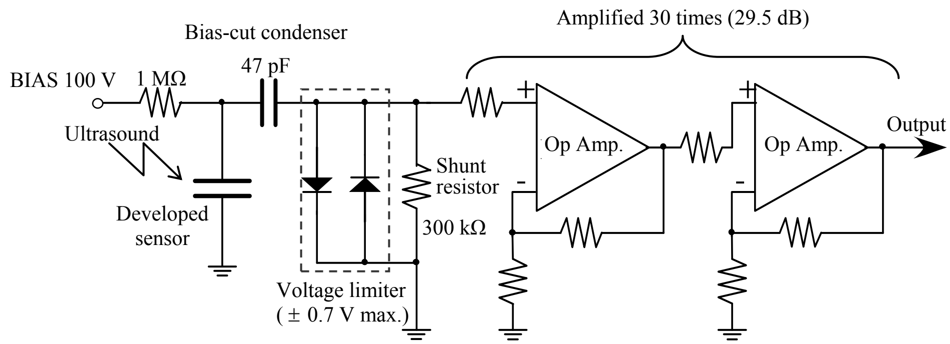


Fig. 15. CV transforming and amplifying circuit.

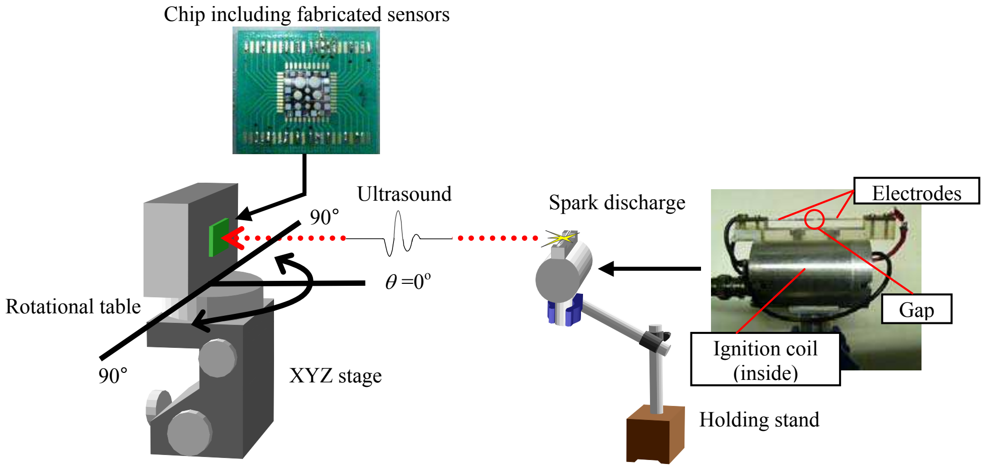


Fig. 16. Experimental condition for characterizing receiving performance.

Transmitted ultrasound is impulsive, the power spectrum of which is distributed over a broad frequency range (Aoyagi et al., 1992). The developed Parylene sensor was set on a rotational table. The distance between the transmitter and the sensor was set to 150 mm. As a reference, a microphone to estimate the sound pressure at the same position where the sensor was set, B&K type 4138 (already detailed in Section 1) was used.

### 4.3 Received pulse waveform, sensitivity, and resonant frequency of one sensor

An example of an ultrasonic pulse waveform received by the developed sensor, whose radius is 1,200 μm, is shown in Fig. 17. In this figure, the waveform received by the B&K microphone is also shown for reference. In the output signal of the developed sensor, there was electrical noise caused by the spark discharge, which could be suppressed by shielding the circuit completely in the future.

Considering that the sensitivity of the B&K microphone is 0.9 mV/Pa, and that the gain of amplification for the developed sensor is 30, the open-circuit sensitivity of the developed sensor was estimated to be 0.4 mV/Pa. The value of typical commercial microphone is in the range from 1 to 50 mV/Pa for the audio range (Brüel & Kjær, 1982; Knowles Acoustics,

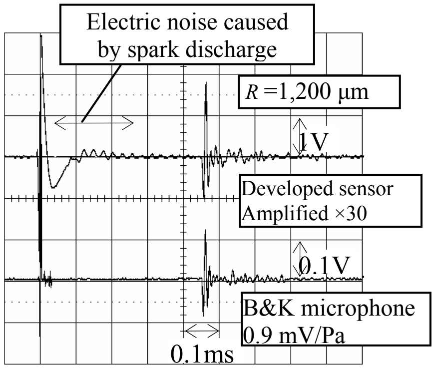


Fig. 17. Received ultrasonic waveforms by developed sensor and reference microphone.

2002). Considering that the diaphragm of the developed sensor is smaller than that of a commercial microphone, the realized sensitivity is reasonable. In the end, the high sensitivity, the order of which is comparable with the B&K microphone, was achieved.

In this study, the resonant frequency is defined as the reciprocal of the period between the first negative peak and the second one of the received waveform in a time domain, as shown in Fig. 18(a). An example of the power spectrum of the received waveform is shown in Fig. 18(b), which was obtained using a fast Fourier transform (FFT) analyzer. The resonant frequency measured based on the definition shown in Fig. 18(a) coincides well with the peak frequency in Fig. 18(b), which is 43 kHz in the case of the sensor used. This value agrees well with FEM simulated value, as shown in Fig. 7, in which experimental data of resonant frequency of the developed sensors having different diaphragm sizes are plotted.

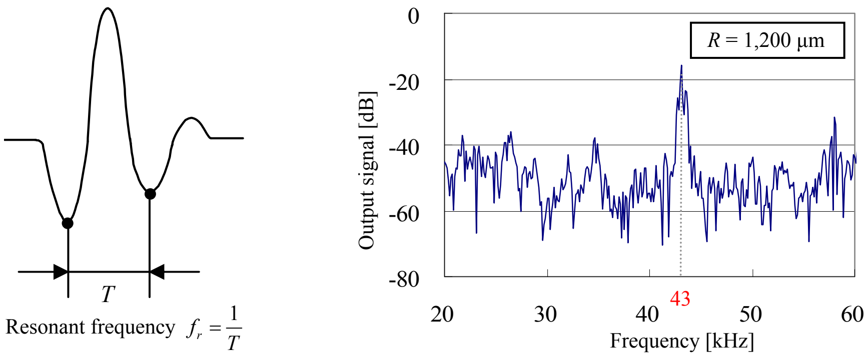


(a) Definition of resonant frequency in time domain (b) Power spectrum of received waveform

Fig. 18. Measurement of resonant frequency.

### 4.4 Fidelity for sound pressure and damping ratio

The developed sensors with different sized acoustic holes, whose diaphragm radius is 1,200 µm, were employed. The radius of an acoustic hole ($r$) was 80, 65 or 50 µm. The ultrasonic pulse waveforms received by the sensors are shown in Figs. 19(a)-(c). To estimate the fidelity, three waveforms for each sensor are shown. The waveform received by the B&K microphone is also shown in Fig. 19(d) for reference.

The three waveforms in Fig. 19(a) resemble each other, as do those in Figs. 19(b) and (c). Thus, the reproducibility of the waveforms is good. In case that $r$ is 80 μm, the residual vibration of the waveform is seen, whereas there are no residual vibrations, i.e., the waveform is well damped, in case that $r$ is 65 and 50 μm. According to the FEM simulation results already shown in Fig. 9, the $\zeta$ values are 0.7, 1.0, and 1.1 for $r$ values of 80, 65, and 50 μm, respectively. When $\zeta$ exceeds 1.0, there are no residual vibrations theoretically, which does not strongly contradict the experimental results, as shown in Figs. 19(b) and (c).

The waveforms received by the developed sensors shown in Figs. 19(b) and (c) coincide well with that received by the B&K microphone shown in Fig. 19(d), which confirms the high fidelity of the developed sensor for sound pressure in the ultrasonic frequency range, provided that an appropriate damping is given to it.

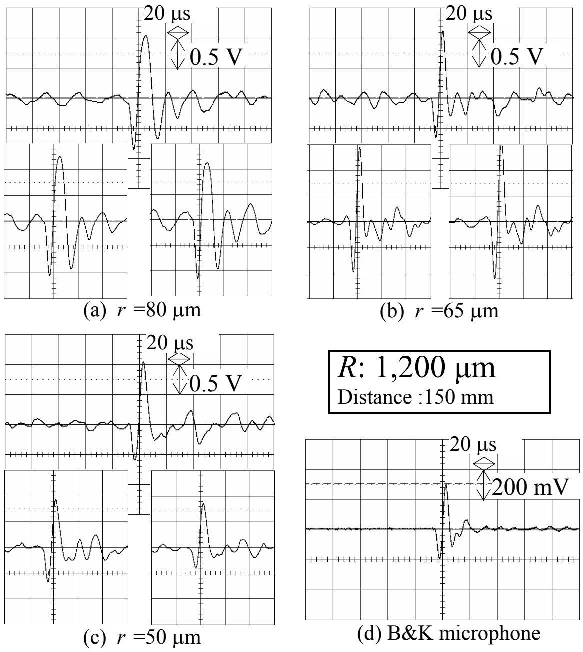


Fig. 19. Received ultrasonic pulse waveforms by changing the radius $r$ of acoustic hole.

### 4.5 Distance measurement

The distance is measured by multiplying the arrival time of the first zero-cross point of the ultrasonic pulse by the sound velocity of 343.6 m/s (at 20°C), as shown in Fig. 20. This point is stable and gives high resolution to the ranging system even when the amplitude varies according to the change in the distance. The sensor, whose diaphragm radius is 1,200 μm, was used. By changing the distance between the transmitter and the developed sensor, the arrival time was measured. The results for distance from 0 to 1,000 mm are shown in Fig. 21.

The measured arrival time shows good linearity with the distance of the source, and error is within 0.1 % of the full range, i.e., this ranging system can detect the distances up to 1 m with an error of less than 1 mm. This ranging system could be effective for mobile robot devices for purposes such as detecting obstacles and recognizing the environment.

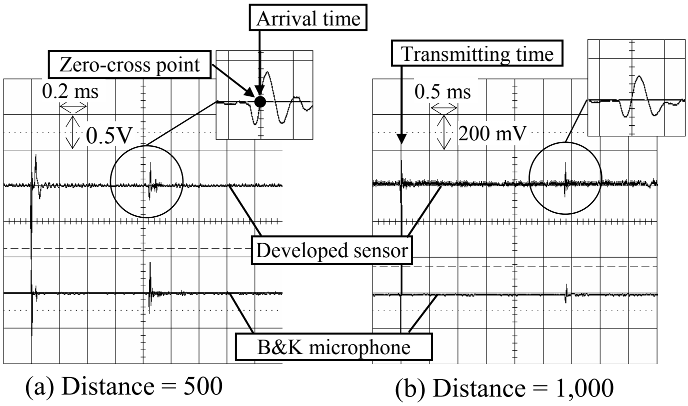


Fig. 20. Distance measurement by multiplying arrival time of zero-cross point by sound velocity.

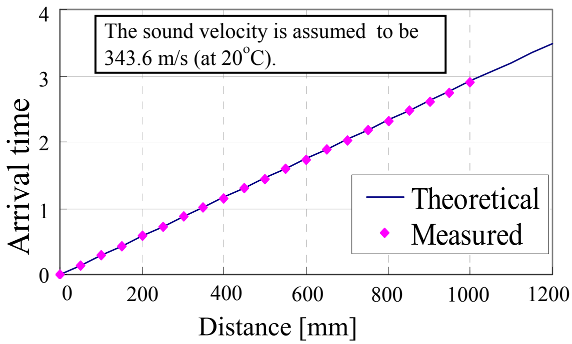


Fig. 21. Relationship between distance and measured arrival time.

### 4.6 Receiving directivity of one sensor

The directivity of the developed sensor was estimated using the experimental setup as already shown in Fig. 16. The peak voltage of received pulse waveform was estimated by changing the angle of the sensor using a rotational table. Results are shown in Fig. 22. From these results, the directivity becomes wide as the diaphragm radius decreases, which implies that miniaturizing the sensor size by micromachining is useful for achieving wide directivity.

It was confirmed that all the sensors used in this experiment can receive ultrasound from a wide area, which ranges from $\theta$=-80 to 80°, with an attenuation level of less than -6 dB compared with the case $\theta$ =0°, i.e., $\theta_{1/2}$ (see equation (1) in Section 1) is approximately 80°.

This wide directivity is effective for realizing the omnidirectional characteristics of the arrayed device comprising many sensors, the detail of which is explained in the following section.

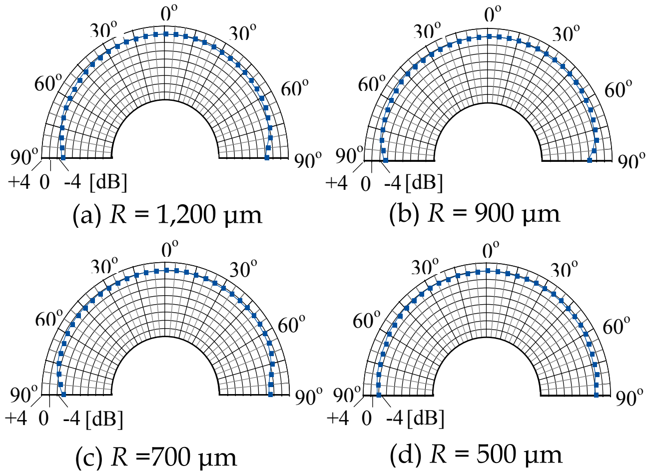


Fig. 22. Receiving directivity of developed sensor.

## 5. Arrayed sensor device and electrical scanning of receiving directivity

### 5.1 Detecting circuitry for capacitance change

An arrayed device comprising 5×5 developed sensors was fabricated. A photograph and its actual size are shown in Fig. 23. The specification of one sensor in the array is as follows: the radius ($R$) of the diaphragm is 1,200 µm, its thickness is 2 µm, the distance between adjacent diaphragms ($a$) is 3,000 µm, the radius of the acoustic hole ($r$) is 60 µm, and the number of holes ($n$) is 121.

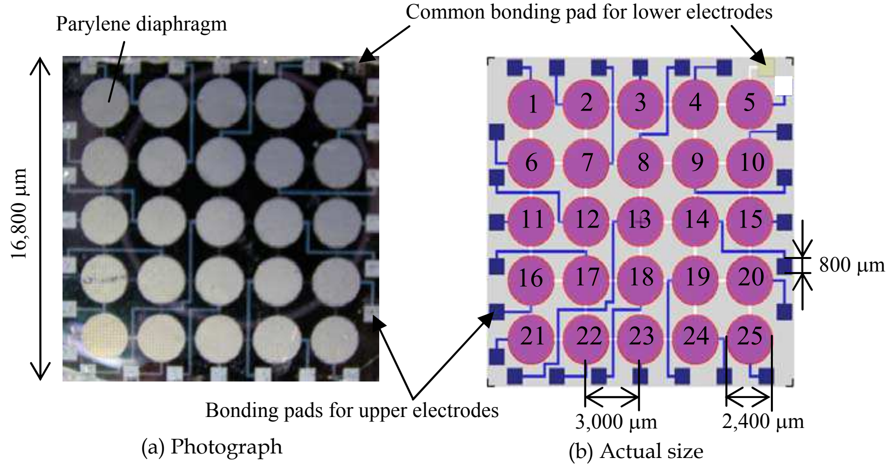


Fig. 23. Fabricated device of ultrasonic sensor array.